

The Role of Nanoparticle Design in Determining Analytical Performance of Lateral Flow Immunoassays

Li Zhan,[†] Shuang-zhuang Guo,[†] Fayi Song,^{||} Yan Gong,[§] Feng Xu,[§] David R. Boulware,[‡] Michael C. McAlpine,[†] Warren C. W. Chan,^{||} and John C. Bischof^{*,†,‡}

[†]Department of Mechanical Engineering, University of Minnesota, 111 Church Street SE, Minneapolis, Minnesota 55455, United States

[‡]Department of Biomedical Engineering, University of Minnesota, 312 Church Street SE, Minneapolis, Minnesota 55455, United States

[‡]Department of Medicine, Microbiology Research Facility (MRF), University of Minnesota, 689 SE 23rd Avenue, Minneapolis, Minnesota 55455, United States

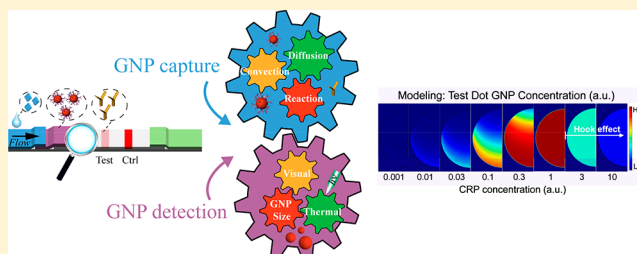
[§]The Key Laboratory of Biomedical Information Engineering of Ministry of Education, School of Life Science and Technology, Bioinspired Engineering and Biomechanics Center (BEBIC), Xi'an Jiaotong University, Xi'an 710049, China

^{||}Institution of Biomaterials and Biomedical Engineering & Terrence Donnelly Center for Cellular and Biomolecular Research, University of Toronto, 160 College Street, Toronto, Ontario 3E1, Canada

Supporting Information

ABSTRACT: Rapid, simple, and cost-effective diagnostics are needed to improve healthcare at the point of care (POC). However, the most widely used POC diagnostic, the lateral flow immunoassay (LFA), is ~1000-times less sensitive and has a smaller analytical range than laboratory tests, requiring a confirmatory test to establish truly negative results. Here, a rational and systematic strategy is used to design the LFA contrast label (i.e., gold nanoparticles) to improve the analytical sensitivity, analytical detection range, and antigen quantification of LFAs. Specifically, we discovered that the size (30, 60, or 100 nm) of the gold nanoparticles is a main contributor to the LFA analytical performance through both the degree of receptor interaction and the ultimate visual or thermal contrast signals. Using the optimal LFA design, we demonstrated the ability to improve the analytical sensitivity by 256-fold and expand the analytical detection range from 3 log₁₀ to 6 log₁₀ for diagnosing patients with inflammatory conditions by measuring C-reactive protein. This work demonstrates that, with appropriate design of the contrast label, a simple and commonly used diagnostic technology can compete with more expensive state-of-the-art laboratory tests.

KEYWORDS: Gold nanoparticles, size dependent, thermal contrast, immunoassay, C-reactive protein



Point-of-care (POC) diagnostics are designed to provide fast and simple measurements to facilitate timely medical decision making to improve clinical outcomes.^{1–3} Although numerous POC tests have been introduced, none are currently able to provide sensitivity and quantitation comparable to laboratory-based diagnostics, such as polymerase chain reaction (PCR) or enzyme-linked immunoassay (ELISA), which constrains their impact.^{4–6} For instance, lateral flow assays (LFAs) have dominated POC diagnostics in the last three decades due to their low cost, simplicity, portability, and robust operation. However, LFAs are approximately 1000-fold lower in sensitivity than alternative laboratory-based techniques.^{7,8} This gap has driven the development of other diagnostic technologies, including paper^{9,10} and chip-based microfluidics,^{11,12} surface plasmon resonance,^{13–15} and biobarcode.^{16,17} Although some of these techniques have achieved comparable sensitivity as PCR or ELISA, they remain in

developmental stages rather than commercial stages for POC applications.^{18,19} An alternative approach, explored here and in other work,^{20–26} focuses on the redesign of LFAs in an attempt to achieve comparable performance to laboratory-based approaches.

During sandwich LFA testing, the analyte flows through the LFA by capillary force and is first captured by detection antibody-labeled spherical gold nanoparticles (GNPs) to form a complex (Figure 1a). This complex is then captured by antibodies on the membrane, leading to accumulation of GNPs at the test site. The test site visually turns red, indicating a positive test, when there are sufficient GNPs present. Traditionally, 30–40 nm diameter GNPs are used as visual

Received: May 31, 2017

Revised: November 7, 2017

Published: November 9, 2017

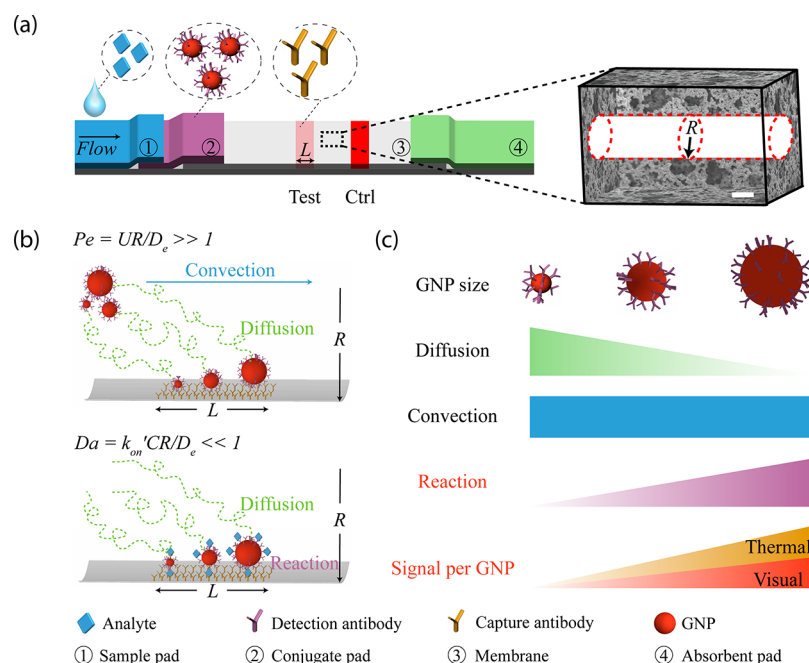


Figure 1. Scaling analysis of the effect of GNP size on LFA sensitivity. (a) Architecture of lateral flow assay with test line width L , assuming that the nitrocellulose membrane is conceptually simplified as bundles of cylindrical pores with radius R ; scale bar is $5\ \mu\text{m}$, Ctrl is the control line of the LFA. (b) Pe is the ratio of diffusion time to convection time of a GNP, where $Pe \gg 1$ in LFA implies the transport of GNP to a test site is diffusion-limited, and Da is the ratio of reaction flux to diffusion flux, where $Da \ll 1$ in LFA implies the rate limit of GNP capture at the test site is reaction (details in Supporting Information section 8). (c) Comparison of 30, 60, and 100 nm diameter GNPs indicates 100 nm GNPs can improve LFA sensitivity due to higher reaction rate and signal per GNP.

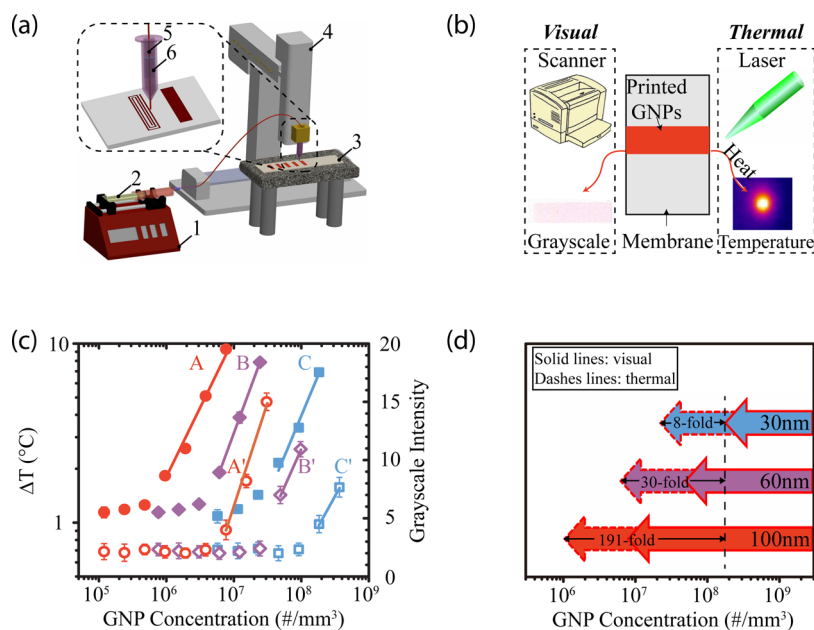


Figure 2. Visual and thermal detection of GNPs of different sizes. (a) GNPs were printed onto a membrane using a 3D printer: 1, syringe pump; 2, syringe; 3, membrane; 4, 3D printer; 5, capillary tube; 6, rubber to fix the capillary tube. (b) Visual and thermal detection methods of printed GNPs. (c) Quantitative thermal and visual detection of 30, 60, and 100 nm diameter GNPs, where A and A' stand for 100 nm GNP thermal and visual signal, B and B' for 60 nm GNP thermal and visual signal, and C and C' stand for 30 nm GNP thermal and visual signal, respectively. (d) Thermal and visual detection limits of printed 30, 60, and 100 nm diameter GNPs.

labels in LFAs; however, LFAs suffer from low GNP capture rate ($<5\%$)^{24,27} and low GNP visual contrast detection, leading to suboptimal sensitivity.²⁸ Approaches to improve label capture and/or label detection have been developed. For instance, new contrast labels including quantum dots,²² upconverting phosphor reporters,²⁰ magnetic particles,^{29,30}

and surface-enhanced Raman scattering GNPs²⁵ have all been applied. Isotachopheresis²⁴- and dialysis²⁶-based sample treatments can preconcentrate analyte and improve label capture. Signal amplification methods such as silver enhancement²¹ and enzyme catalytic amplification²³ have also been explored. These improvements in LFA performance lead to additional cost,

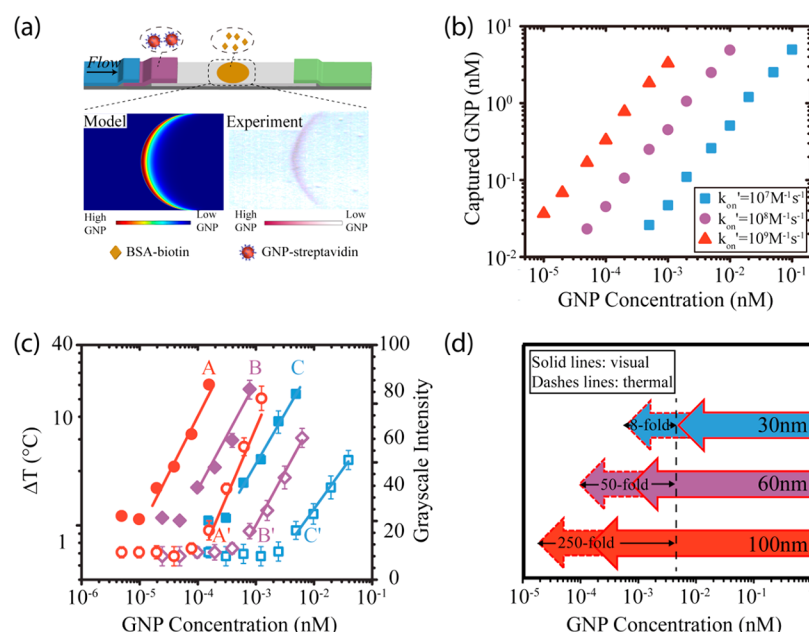


Figure 3. Larger-size GNPs can be detected at lower concentrations in streptavidin/biotin direct binding LFAs. (a) Schematics of streptavidin/biotin LFAs. The experimental and modeling results of the LFA test showed GNPs were captured at the front arc of the test dot. (b) Modeling results of quantitative 30 nm GNP capture for different effective forward reaction constant values. (c) Experimental thermal and visual signals of 30, 60, and 100 nm diameter GNP streptavidin/biotin LFAs; A and A' stand for 100 nm GNP thermal and visual signal, B and B' for 60 nm GNP thermal and visual signal, and C and C' stand for 30 nm GNP thermal and visual signal, respectively. (d) Experimental thermal and visual detection limits of streptavidin/biotin LFAs with 30, 60, and 100 nm diameter GNPs.

labor, complexity, or loss of portability that may hinder point-of-care deployment.

In our previous studies, we developed a thermal contrast amplification (TCA) reader to read the thermal signal of commercial LFAs.^{28,31} The TCA reader collects the temperature changes of GNPs upon laser irradiation in the test site and provides improved sensitivity (8-fold) and quantitation of the analyte over traditional visual reading of the commercial LFAs built with ~30 nm GNP contrast.³¹ Here, we shift focus to redesign the LFA for improved analytical performance using the thermal contrast reader. Our goal is to assess whether redesign of the LFAs for thermal contrast can achieve competitive analytical performance with laboratory techniques. To achieve this, we first modeled the entire process and identified important parameters such as GNP size and concentration, reaction rate constant (antibody binding), and flow speed (reaction time) that determine the limit of detection of the thermal signal from the LFAs. We then tested the findings from the model with experiments to achieve a 256-fold higher analytical sensitivity with thermal contrast than traditional 30 nm GNP LFA visual contrast, thereby achieving a range of C-reactive protein (CRP) detection comparable to that of ELISA-based laboratory diagnostics. Specifically, we chose to study the impact of nanoparticle size on GNP detection and capture as they relate to the analytical performance of the LFA. Larger size GNPs with 60 and 100 nm diameters were introduced in addition to the traditional 30 nm GNPs. The larger size GNPs exhibit higher reaction affinity as they carry more antibodies, thus increasing GNP capture (Figure 1c). In addition, the larger-size GNPs have stronger light absorption and scattering properties, thus improving GNP detection (Figure S1). Importantly, the modeling and experimentation processes presented here can be used in the future to optimize the analytical performance of other

nanoparticle-based assays such as microfluidic, biobarcode detection, and so forth.^{9–12,16,17}

To study the detection sensitivity of different sized GNPs, we needed to deposit citrate-stabilized GNPs (30, 60, and 100 nm diameters) onto the LFA membrane uniformly, quantitatively, and without aggregation. The pipettes and Epson XP310 inkjet printers were used but resulted in nonuniform “coffee rings” and unacceptable aggregation, respectively (Figure S2). For this to be addressed, GNPs were washed and dispersed in 65% (w/w) glycerol and printed using a 3D printer and syringe pump to achieve uniformity and quantitation (Figure 2a, method details in Supporting Information section 4).³² The monodisperse (i.e., nonaggregated) status of printed GNPs was confirmed with scanning electron microscopy (Figure S3). After printing at known GNP concentrations, pumping rate, and printing time, we used a scanner (Epson X310) and a TCA reader to calibrate the visual (i.e., grayscale intensity) and thermal (i.e., temperature change) signals, respectively, of the deposited GNPs (Figure 2b). The quantitation of GNP amount vs visual or thermal detection is presented in Figure 2c. For instance, 24- and 191-fold sensitivity improvement for visual and thermal detection of 100 nm GNPs over visual detection of 30 nm GNPs is shown in Figure 2d. The visual and thermal detection thresholds of different-sized GNPs are listed in Table S1. Additionally, this 3D printing technique can serve as a platform to quantitatively study and compare the laser heating (i.e., thermal performance) of different types of nanoparticles such as gold nanocubes, gold nanorods, and others.

We next used scaling and modeling, followed by experimentation, to investigate the impact of nanoparticle size in GNP capture. We studied two LFA cases: case 1, diffusion, convection, and direct GNP binding LFA (biotin–streptavidin); case 2, diffusion, convection, and sandwich GNP binding LFA with CRP as analyte.

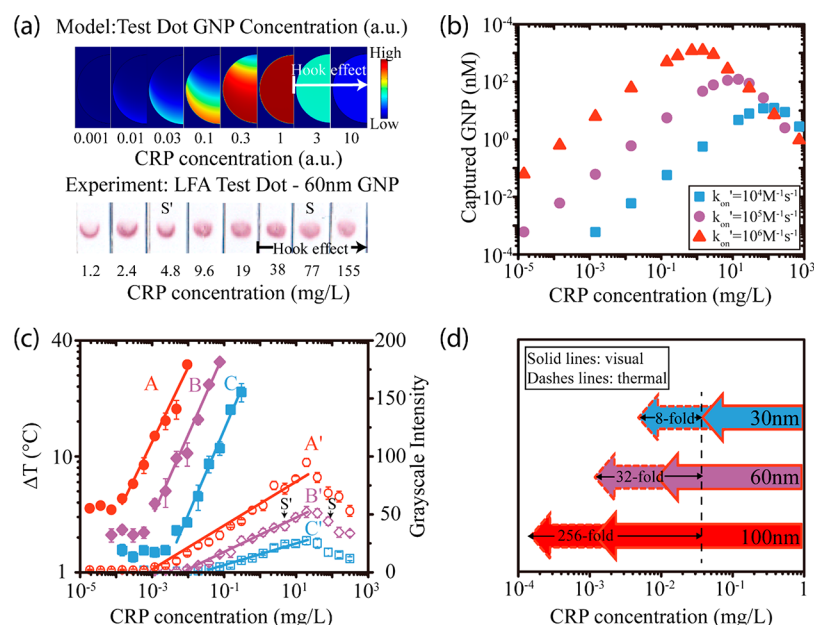


Figure 4. Combination of 100 nm GNPs and TCA reader provides 256-fold sensitivity improvement in CRP LFAs. (a) Modeling and experimental results of test dot visual reading and ability to compensate for the “hook” effect observed in all LFAs at very high concentrations. (b) Modeling results of quantitative 30 nm GNP capture for different effective forward reaction rate constant values. (c) Experimental visual and thermal signals of CRP LFAs; A and A’ stand for 100 nm GNP thermal and visual signal, B and B’ for 60 nm GNP thermal and visual signal, and C and C’ stand for 30 nm GNP thermal and visual signal, respectively. (d) Experimental thermal and visual detection limits of CRP LFAs with 30, 60, and 100 nm diameter GNPs.

To begin, we scaled the Peclet number (Pe) and the Damkohler number (Da) for these cases to assess the importance of diffusion to convection and reaction in the LFAs (Figure 1b). The nitrocellulose membrane is conceptually simplified as a bundle of cylindrical pores of radius R (Figure 1a).³³ The Peclet number ($Pe = UR/D_e$), the ratio of diffusion time to convection time of a GNP with effective diffusivity D_e , was calculated, where U is the convective velocity (Figure 1b). A further calculation of the Damkohler number ($Da = k_{on}'CR/D_e$) compares the reaction flux (of a given test site capture antibody concentration C) to diffusion flux (Figure 1b). Here, the effective forward reaction rate constant (k_{on}') for antibody-labeled GNPs is assumed to be²⁷

$$k_{on}' = nk_{on} \quad (1)$$

where k_{on} is the forward rate constant for a single antibody–antigen interaction in the LFA membrane environment, and n is the effective number of antibodies per GNP. With the calculated $Pe \gg 1$ (convection dominates diffusion) and $Da \ll 1$ (diffusion dominates reaction) shown in Table S2; thus, the reaction is the rate-limiting step to improve GNP capture (details in Supporting Information section 8). We hypothesize that larger-sized GNPs (60 and 100 nm) could improve GNP capture as n increases in eq 1 due to larger surface area (Figure 1c).

We then developed a COMSOL model to extend the above scaling analysis and predict LFA performance prior to experiments, thereby guiding LFA design for both cases (Supporting Information section 8). We performed a parametric study to assess the impact of varying the convective velocity as well as GNP diffusivity and effective forward rate constant on GNP capture using the parameters listed in Table S3. The model shows that reaction and convection have a higher impact on GNP capture than diffusion (Figures S4 and S5). Indeed, reaction and convection are linked as reducing

velocity increases the time for reaction (i.e., residence time in the test site), underscoring again that reaction is the rate-limiting phenomenon in GNP capture. In addition, we studied the impact of GNP concentration used in the conjugate pad on the final test line signal (i.e., captured GNP amount) using the model. The model shows that, as the GNP concentration increases, the test line captured GNP amount will first increase and then reach a plateau (Figure S6). The modeling helps to identify key parameters such as GNP size and concentration, reaction rate constant, and flow speed that determine the analytical performance of LFAs.

In case 1, we used COMSOL to model direct binding of streptavidin-coated GNPs to the test dot coated with excess biotin (Figure 3a). The model predicted that the majority of the GNPs are captured at the front arc of the test dot due to high binding affinity ($K_d = 10^{-14}$ M) of the excess biotin to the streptavidin (Figure 3a). In Figure 3b, the model showed that the GNP capture increases as k_{on}' increases, indicating sensitivity improvement with larger GNP (larger k_{on}'). Importantly, because of the enhanced capture of larger size GNPs, we expect greater sensitivity improvement between visual detection of 30 nm GNP and thermal detection of 100 nm GNP in a binding LFA (i.e., cases 1 and 2) vs printed GNPs in the membrane where no GNP binding exists (Figure S7).

To experimentally test case 1 model predictions, we conjugated streptavidin to GNPs to bind a test dot coated with excess biotin in the LFA. We tested different concentrations of streptavidin-coated GNPs. As predicted by the model, only a red arc at the test dot edge was observed after an LFA test (Figure 3a, Figure S8). The quantitative correlation between GNP concentration and thermal signal ($R^2 = 0.96$) as well as visual signal ($R^2 = 0.95$) are presented in Figure 3c. A 250-fold improvement in sensitivity is illustrated in Figure 3d for thermal detection of 100 nm GNP over visual detection of 30 nm GNP. Although Figure S4 demonstrates trends for our

model, absolute agreement between the model and experimental results requires fitting certain parameters, most importantly, the reaction term. We fitted k_{on}' of different-sized GNPs using the thermal signal (ΔT) of test dots and the “ ΔT to GNP concentration” calibration curves (Figure 2c, Figure S9). The results indicate that 100 nm GNPs have more than 3-fold higher k_{on}' than 30 nm GNPs (2.5×10^7 vs $7.5 \times 10^6 \text{ M}^{-1} \text{ s}^{-1}$), implying that larger GNPs have higher n in eq 1.

In case 2, we used COMSOL to model sandwich binding of GNP in the test dot of a CRP LFA. We noted different test dot patterns for different CRP concentration, indicating semi-quantitative visual readings (Figure 4a). We showed that these test dot patterns can be used to expand the LFA analytical range beyond the “hook” effect, which occurs at excessively high analyte concentrations, leading to a reduction in GNP capture.³⁴ For instance, just before and after the “hook” effect, one visual signal value can be related to two different analyte concentrations, i.e., S and S' in Figure 4c. The model predicted different test dot patterns such that we can distinguish S (after the “hook” effect) from S' (before the “hook” effect), albeit they have the same visual signal averaged across the dot (Figure 4a, c). Importantly, the model also revealed that this approach requires $k_{\text{on}}' > 10^3 \text{ M}^{-1} \text{ s}^{-1}$, which suggests a failure criterion when using low affinity antibodies or sparsely coated GNP labels (Figure S10). The sensitivity and linear quantitation range (before the “hook” effect) of the LFA also depends on k_{on}' (Figure 4b). Specifically, a higher effective forward rate constant increases GNP capture and therefore LFA sensitivity. Using the thermal detection limit of 100 nm GNPs ($1.6 \times 10^{-3} \text{ nM}$, Table S1), a $>4 \log_{10}$ linear visual detection range could be expected when $k_{\text{on}}' = 10^4 \text{ M}^{-1} \text{ s}^{-1}$, whereas the linear detection range increases to $>5 \log_{10}$ when $k_{\text{on}}' = 10^5 \text{ M}^{-1} \text{ s}^{-1}$ (Figure 4b).

Finally, we experimentally evaluated whether the improvements in direct binding LFAs (case 1) could be extended to sandwich LFA (case 2). We constructed a sandwich LFA to detect CRP, an important clinical biomarker of inflammation.³⁵ A point-of-care quantitative CRP assay would be highly useful to distinguish bacterial from viral infections to guide antibiotic use considering that the current multiple hour turnaround time for a laboratory-based CRP assay is impractical in an outpatient setting to affect medical decision making.³⁶ To allow quantitative comparison between different size GNP LFAs, we used the same number of GNPs per LFA (i.e., 6×10^8). We performed dilution testing with standard human CRP reference. The different patterns of test dot binding (bottom to top in flow) as predicted by the model enable the detection before and after the “hook” effect (Figure 4a). This effectively extends the visual analytical range to $5 \log_{10}$ (10^{-3} to $>10^2 \text{ mg/L}$) using 100 nm GNPs (Figure 4c, Table S4). Further, thermal contrast achieves one \log_{10} sensitivity improvement over visual contrast for all GNP sizes, including 30 nm as previously shown in commercial LFAs.³¹ Therefore, $6 \log_{10}$ detection range (10^{-4} to $>10^2 \text{ mg/L}$) in CRP LFA was demonstrated with 100 nm GNP and a TCA reader. In sum, the 100 nm GNP yields a 256-fold sensitivity improvement using thermal detection versus traditional 30 nm GNP visual detection (Figure 4d, Figure S11). In the future, another \log_{10} improvement using TCA with different-shaped nanoparticles such as nanorods or nanoshells with thermal contrast detection may be possible.²⁸

To improve translation and demonstrate clinical use, we also tested a human serum sample. The results aligned well with the calibration curves obtained with standard human CRP

reference samples (Figures S12 and S13). Similar to case 1, we found 100 nm GNPs have a more than 2-fold higher k_{on}' than 30 nm GNPs (6.5×10^4 vs $2.8 \times 10^4 \text{ M}^{-1} \text{ s}^{-1}$, Figure S14). We further noted that the ratio of k_{on}' (100 vs 30 nm GNP) in case 1 is greater than the ratio in case 2. We attribute this to the extra curvature and molecular length that would impede binding in sandwich (case 2) vs direct binding (case 1).

Theoretically, increasing GNP size above 100 nm could further increase LFA sensitivity. However, GNP capture will be rate limited by diffusion ($\text{Da} \gg 1$) as k_{on}' increases with GNP size. Therefore, further increasing GNP size will decrease GNP capture as larger GNPs have slower diffusion rates. In addition, the cost of gold and especially antibodies needed to coat this gold increases dramatically as the GNP size increases (Table S5). Furthermore, we use modeling to demonstrate that larger GNPs (for example: 400 nm) will settle within the pores of the membrane within 50 s, the time necessary for a GNP to travel from conjugate pad to test line (Figure S15, details in Supporting Information section 9). Importantly, this effect will be compounded by the increased chance of nonspecific binding of larger-sized GNP–antibody conjugates to either the test line antibody or background membrane of the assay. Thus, although larger GNPs can improve the limit of detection, they may also cause false positive results that decrease the accuracy of detection (details in Supporting Information section 9). Thus, for GNPs beyond 100 nm, the detection accuracy is considered more important than simply achieving higher sensitivity (i.e., limit of detection). We expect that this trade-off will yield a unique maximum GNP size limit depending on antibody selection, membrane selection, and tolerance of false positives for any newly designed assays. Further, directly measuring k_{on}' of GNPs within LFA environments using radioactively labeled antibodies will be useful to improve the model and find the ultimate limits of this LFA technology.²⁷

In conclusion, we studied how GNP design, specifically size and contrast (visual vs thermal), affects LFA analytical performance. We scaled and modeled the transport and reaction processes in the LFA. We found that the sensitivity greatly depends on the GNP binding process. Our model can predict LFA performance based on nanoparticle design, thus helping to reduce excessive experimentation and more quickly identify and experimentally verify optimum LFA designs. For instance, our model shows that larger-size GNPs have higher binding affinity and are detected at lower concentration. Using 100 nm GNPs with thermal contrast detection, our LFAs were then experimentally verified to detect CRP over approximately a $6 \log_{10}$ concentration range spanning the range of both laboratory and POC CRP assays on the market in one simple test (Table S6). Thus, the modified GNP labels with both visual and thermal contrast detection show great promise in creating a POC diagnostic platform that is competitive in sensitivity, analytical range, and quantitation with laboratory-based technologies.

■ ASSOCIATED CONTENT

Supporting Information

The Supporting Information is available free of charge on the ACS Publications website at DOI: 10.1021/acs.nanolett.7b02302.

Experimental and simulation methods details, GNP TEM images, and optical properties calculations, comparison of different GNP deposition methods, COMSOL

modeling parameters and results of cases 1 and 2, LFA visual and thermal detection in cases 1 and 2, LFA flow velocity measurement, existing commercial detection methods of CRP, CRP clinical sample test results, and cost of antibody and GNP in CRP LFA (PDF)

AUTHOR INFORMATION

Corresponding Author

*E-mail: bischof@umn.edu.

ORCID

Feng Xu: 0000-0003-4351-0222

Warren C. W. Chan: 0000-0001-5435-4785

John C. Bischof: 0000-0001-6726-7111

Notes

The authors declare no competing financial interest.

ACKNOWLEDGMENTS

This work is supported by Minnesota-Mayo Partnership Grant (J.C.B., D.R.B.), IEM Seed Grant (UM) and Kuhrmeyer Chair to J.C.B. The authors thank Dr. Zhenpeng Qin who helped train Mr. Zhan on thermal contrast, Dr. Zhe Gao for help with SEM imaging, and Kai Wang and Cathlyn Wang for help with the experiments. W.C.W.C. acknowledges the Canadian Institutes of Health Research and Natural Sciences and Engineering Research Council of Canada. F.X. and G.Y. were financially supported by the National Instrumentation Program of China (2013YQ190467). D.R.B. acknowledges the National Institute of Health (R01NS086312). M.C.M. acknowledges the National Institute of Biomedical Imaging and Bioengineering of the National Institutes of Health (Award No. 1DP2EB020537). The content is solely the responsibility of the authors and does not necessarily represent the official views of the National Institutes of Health.

REFERENCES

- (1) Yager, P.; Domingo, G. J.; Gerdes, J. *Annu. Rev. Biomed. Eng.* **2008**, *10*, 107–144.
- (2) Drain, P. K.; Hyle, E. P.; Noubary, F.; Freedberg, K. A.; Wilson, D.; Bishai, W. R.; Rodriguez, W.; Bassett, I. V. *Lancet Infect. Dis.* **2014**, *14*, 239–249.
- (3) Pai, N. P.; Vadnais, C.; Denking, C.; Engel, N.; Pai, M. *PLoS Med.* **2012**, *9*, e1001306.
- (4) Lippa, P. B.; Müller, C.; Schlichtiger, A.; Schlebusch, H. *TrAC, Trends Anal. Chem.* **2011**, *30*, 887–898.
- (5) Gubala, V.; Harris, L. F.; Ricco, A. J.; Tan, M. X.; Williams, D. E. *Anal. Chem.* **2012**, *84*, 487–515.
- (6) Derda, R.; Gitaka, J.; Klapperich, C. M.; Mace, C. R.; Kumar, A. A.; Lieberman, M.; Linnes, J. C.; Jores, J.; Nasimolo, J.; Ndung'u, J. *PLoS Neglected Trop. Dis.* **2015**, *9*, e0003676.
- (7) Hu, J.; Wang, S.; Wang, L.; Li, F.; Pingguan-Murphy, B.; Lu, T. J.; Xu, F. *Biosens. Bioelectron.* **2014**, *54*, 585–597.
- (8) Posthuma-Trumpie, G. A.; Korf, J.; van Amerongen, A. *Anal. Bioanal. Chem.* **2009**, *393*, 569–582.
- (9) Martinez, A. W.; Phillips, S. T.; Whitesides, G. M.; Carrilho, E. *Anal. Chem.* **2010**, *82*, 3–10.
- (10) Byrnes, S.; Thiessen, G.; Fu, E. *Bioanalysis* **2013**, *5*, 2821–2836.
- (11) Yager, P.; Edwards, T.; Fu, E.; Helton, K.; Nelson, K.; Tam, M. R.; Weigl, B. H. *Nature* **2006**, *442*, 412–418.
- (12) Lee, W. G.; Kim, Y.-G.; Chung, B. G.; Demirci, U.; Khademhosseini, A. *Adv. Drug Delivery Rev.* **2010**, *62*, 449–457.
- (13) El-Sayed, I. H.; Huang, X.; El-Sayed, M. A. *Nano Lett.* **2005**, *5*, 829–834.
- (14) Homola, J. *Chem. Rev.* **2008**, *108*, 462–493.
- (15) Mayer, K. M.; Hafner, J. H. *Chem. Rev.* **2011**, *111*, 3828–3857.
- (16) Klostranec, J. M.; Xiang, Q.; Farcas, G. A.; Lee, J. A.; Rhee, A.; Lafferty, E. I.; Perrault, S. D.; Kain, K. C.; Chan, W. C. *Nano Lett.* **2007**, *7*, 2812–2818.
- (17) Nam, J.-M.; Thaxton, C. S.; Mirkin, C. A. *Science* **2003**, *301*, 1884–1886.
- (18) Chin, C. D.; Linder, V.; Sia, S. K. *Lab Chip* **2012**, *12*, 2118.
- (19) Bissonnette, L.; Bergeron, M. G. *Clin. Microbiol. Infect.* **2010**, *16*, 1044–1053.
- (20) Hampl, J.; Hall, M.; Mufti, N. A.; Yao, Y.-m. M.; MacQueen, D. B.; Wright, W. H.; Cooper, D. E. *Anal. Biochem.* **2001**, *288*, 176–187.
- (21) Shyu, R.-H.; Shyu, H.-F.; Liu, H.-W.; Tang, S.-S. *Toxicol.* **2002**, *40*, 255–258.
- (22) Li, Z.; Wang, Y.; Wang, J.; Tang, Z.; Pounds, J. G.; Lin, Y. *Anal. Chem.* **2010**, *82*, 7008–7014.
- (23) He, Y.; Zhang, S.; Zhang, X.; Baloda, M.; Gurung, A. S.; Xu, H.; Zhang, X.; Liu, G. *Biosens. Bioelectron.* **2011**, *26*, 2018–2024.
- (24) Moghadam, B. Y.; Connelly, K. T.; Posner, J. D. *Anal. Chem.* **2015**, *87*, 1009–1017.
- (25) Fu, X.; Cheng, Z.; Yu, J.; Choo, P.; Chen, L.; Choo, J. *Biosens. Bioelectron.* **2016**, *78*, 530–537.
- (26) Tang, R.; Yang, H.; Choi, J. R.; Gong, Y.; Hu, J.; Feng, S.; Pingguan-Murphy, B.; Mei, Q.; Xu, F. *Talanta* **2016**, *152*, 269–276.
- (27) Mosley, G. L.; Nguyen, P. T.; Wu, B.; Kamei, D. *Lab Chip* **2016**, *16*, 2871–2881.
- (28) Qin, Z.; Chan, W. C.; Boulware, D. R.; Akkin, T.; Butler, E. K.; Bischof, J. C. *Angew. Chem.* **2012**, *124*, 4434–4437.
- (29) Ruiz-Vega, G.; Kitsara, M.; Pellitero, M. A.; Baldrich, E.; del Campo, F. J. *ChemElectroChem* **2017**, *4*, 880–889.
- (30) Liu, C.; Jia, Q.; Yang, C.; Qiao, R.; Jing, L.; Wang, L.; Xu, C.; Gao, M. *Anal. Chem.* **2011**, *83*, 6778–6784.
- (31) Wang, Y.; Qin, Z.; Boulware, D. R.; Pritt, B. S.; Sloan, L. M.; González, I. J.; Bell, D.; Rees-Channer, R. R.; Chiodini, P.; Chan, W. C.; Bischof, J. C. *Anal. Chem.* **2016**, *88*, 11774–11782.
- (32) Soltman, D.; Subramanian, V. *Langmuir* **2008**, *24*, 2224–2231.
- (33) Adler, P. *Porous Media: Geometry and Transport*, New York **1992**, 4–5.
- (34) Bahadır, E. B.; Sezgentürk, M. K. *TrAC, Trends Anal. Chem.* **2016**, *82*, 286–306.
- (35) Ridker, P. M.; Hennekens, C. H.; Buring, J. E.; Rifai, N. N. *Engl. J. Med.* **2000**, *342*, 836–843.
- (36) Lin, S.-C.; Tseng, C.-Y.; Lai, P.-L.; Hsu, M.-Y.; Chu, S.-Y.; Tseng, F.-G.; Cheng, C.-M. *Sci. Rep.* **2016**, *6*, 38171.